Catalysis Science & Technology

PAPER

View Article Online
View Journal | View Issue

Cite this: *Catal. Sci. Technol.*, 2019, 9, 2578

Tunable colloidal Ni nanoparticles confined and redistributed in mesoporous silica for CO_2 methanation†

Wilbert L. Vrijburg, [a] Jolanda W. A. van Helden,[a] Arno J. F. van Hoof, [a] Heiner Friedrich, [a] Esther Groeneveld,[b] Evgeny A. Pidko ‡*[a] and Emiel J. M. Hensen *[a]

Herein we report our efforts to control the size of colloidal Ni nanoparticles (NiNPs) *via* a seed-mediated approach and to produce supported Ni catalysts that are sinter-resistant. NiNPs are prepared using a mild capping ligand and an external reducing agent at 90 °C to obtain seeds of 3–4 nm, followed by NiNP growth at 220 °C to vary the final size up to 8 nm. These NiNPs were either introduced onto high surface area silica *via* direct deposition in organic solvents, or encapsulated in mesoporous silica. Encapsulation was determined to be the most promising approach to support the particles. A range of such encapsulated NiNP catalysts were evaluated for CO_2 hydrogenation between 200–400 °C: they were comparably active as catalysts reported in the literature, and thermally stable and sinter-resistant for 70 h at 350 °C. Nevertheless, it was found that the Ni phase was redistributed throughout the mesoporous silica network, resulting in Ni catalysts with nearly identical particle size of 4–5 nm, determined by the size of the support pores, after a combination of oxidative and reductive pretreatments. Our approach provides a route to obtain Ni@SiO_2 catalysts with a narrow particle size distribution from a range of colloidal NiNP precursors.

Received 17th March 2019,
Accepted 19th April 2019

DOI: 10.1039/c9cy00532c

rsc.li/catalysis

1 Introduction

Colloidal routes towards supported metal catalysts have long been proposed as a strategy to obtain well-defined heterogeneous catalysts due to the possibility to control nanoparticle size and shape.[1,2] The flexibility in colloidal preparation routes are often viewed as advantageous over conventional catalyst synthesis methods such as impregnation or coprecipitation.[3,4] Both particle size and shape are known to significantly influence the catalytic activity of supported nanoparticles in structure–sensitive reactions such as Fischer–Tropsch and CO_2 reduction.[5–9] Despite the perceived advantages for colloidal synthetic approaches, most studies have focused on producing noble metal catalysts,[10] with industrially relevant metals such as Ni and Co receiving limited attention.

The synthesis of supported metal catalysts *via* colloidal approaches involves two main challenges related to (i) the control of the nanoparticle size and (ii) the controlled deposition of the colloidal nanoparticles onto a support and the removal of the capping ligands to obtain active catalysts. The former challenge has received more attention than the latter, even though the deposition step is crucial to obtain active and stable catalysts.[11] Ineffective anchoring of the nanoparticles may lead to significant particle aggregation during high-temperature activation, whereas low temperature treatments may not effectively remove the capping ligands.[12,13] Good control over nanoparticle deposition on oxidic supports is particularly important for Ni, which is susceptible to particle sintering. Moreover, despite several studies in recent years aiming to control Ni nanoparticle (NiNP) size, only limited studies have provided synthetic approaches that yielded NiNPs between 1–10 nm, which that were then also deposited on a support to investigate particle sintering after capping agent removal.[14]

Colloidal nanoparticles are comprised of a metallic core stabilized by long-chain organic ligands (capping/stabilizing agents). Vital to obtaining homogeneously dispersed nanoparticles are homogeneous seed formation (nucleation) of metallic monomers, induced by metal atom (monomer) concentrations surpassing a threshold concentration (supersaturation). Nucleation stops once the monomer concentration

[a] *Laboratory of Inorganic Materials and Catalysis, Schuit Institute of Catalysis, Eindhoven University of Technology, P.O. Box 513, 5600 MB Eindhoven, The Netherlands. E-mail: e.a.pidko@tudelft.nl, e.j.m.hensen@tue.nl*
[b] *BASF Nederland B.V., De Meern, The Netherlands*

† Electronic supplementary information (ESI) available: Synthesis procedures and additional material characterization including TEM, XPS (quantification and sputtering results), TGA profiles, N_2 physisorption isotherms, and HAADF-STEM images. See DOI: 10.1039/c9cy00532c

‡ Present address: Inorganic Systems Engineering group, Department of Chemical Engineering, Delft University of Technology, Van der Maasweg 9, 2629 HZ, Delft, The Netherlands.

drops below the supersaturation concentration, with existing nuclei consuming the remaining monomers in the organic solution (heterogeneous nucleation).[15] Synthetic routes to produce NiNPs have usually involved either (i) thermal decomposition of an organometallic precursor to produce and grow the nuclei, or (ii) inducing nucleation using an external reducing agent to reduce Ni^{2+}, either as organometallic complex or salt, to metallic Ni^0. In thermal decomposition procedures, Ni is usually reduced by the capping agents present in the solution.[16]

Thermal decomposition methods for NiNP synthesis have been extensively explored, with $Ni(acac)_2$ often employed as the Ni precursor. Zhang *et al.* studied the influence of temperature on NiNP size employing only oleylamine (OAm) as both solvent and capping agent.[17] Polydispersed particles with a mean diameter of 22 nm were obtained after nucleation and growth at 220 °C, while nucleation was already found to start at 180 °C. A narrow particle size distribution for 20–60 nm NiNPs could be obtained by separating the seed and growth steps in the synthesis. To achieve this, a two-step seed-growth approach was introduced, in which the initial seeds formed at 220 °C could be grown more homogeneously by introducing additional precursor at room temperature and then maintaining the solution at 195 °C. Chen *et al.* explored a variety of alkylamines as capping agents and reducing agents when preparing NiNPs *via* thermal decomposition routes, obtaining particles between 10–50 nm.[18]

In order to improve control over particle sizes, many studies resorted to stronger capping agents. These have primarily involved phosphorous containing ligands,[18–23] although sulfur containing agents have also been explored.[24,25] Winnischofer *et al.* screened various ratios of Ni precursors, phosphine, and amine functionalized ligands to control Ni particle sizes between 4.8–16.3 nm.[26] Carenco *et al.* studied the growth mechanism of NiNPs, employing a combination of trioctylphosphine (TOP) and OAm as capping agents.[19] Within their work, the authors determined OAm to be an effective reducing agent (and therefore nucleation agent) but a weak capping agent, whereas the phosphine ligand was an efficient capping agent but poor reducing agent for $Ni(acac)_2$. The exclusive use of OAm as both capping and reducing agent led to Ni particles between 50–80 nm under thermal reduction conditions. Their understanding of the nucleation and growth mechanism allowed the authors to tailor particle sizes from 2 to 30 nm by varying the OAm : TOP ratio, with TOP-only mixtures yielding the smallest particle sizes with a mean diameter of 2 nm.

The key problem with employing phosphorous containing ligands (P-ligands) is that the phosphorous is inevitably incorporated into the Ni lattice, even at temperatures below 220 °C.[19,27–29] Calcination at 500 °C was found to be insufficient to remove phosphorous from deposited NiNPs, yielding supported P-containing Ni nanoparticles which were inactive in cyclohexene hydrogenation.[30] However, Ni-phosphides were not observed by XRD and the predominant phase in the synthesized NiNPs was metallic Ni. Similar effects have also been observed for Co-based NPs.[31] The use of P-containing ligands should therefore be avoided if Ni- and Co-based hydrogenation catalysts are desired.

Thermal decomposition strategies alone are insufficient to achieve particle size control in the absence of P-ligands, particularly if $Ni(acac)_2$ is employed as the Ni precursor. In addition to thermal reduction strategies the use of strong reducing agents such as $NaBH_4$,[32,33] hydrazine,[34–36] polyols,[37] and more recently borane *tert*-butylamine (BTB) complex have been explored.[38,39] Using OAm and oleic acid (OAc) as co-surfactants at 90 °C, Metin and co-workers were able to synthesize monodisperse NiNPs from 3.2 to 5.4 nm by lowering the BTB/Ni ratio from 3/1 to 1/1 respectively.[38] Particles smaller than 3 nm were obtained by Li *et al.* by increasing the temperature at which BTB was injected into the $Ni(acac)_2$ solution from 90 °C to 180 °C.[40] However, particle size control to obtain a series of larger particles between 4 to 10 nm was not achieved, which could be desirable when employed in structure–sensitive catalytic reactions such as CO and CO_2 hydrogenation.[5–8]

In addition to accurately controlling the particle size of colloidal NiNPs, their effective and controlled deposition on oxidic supports and subsequent removal of the organic ligands are vital to obtain active and well-defined catalysts. Direct deposition *via* impregnation methods are facile,[1] but Ni is prone to sintering during ligand removal by calcination at elevated temperatures.[30] Rinaldi *et al.* deposited NiNPs on SiO_2 and found that high temperature treatments, although effective at reducing the amount of ligands on the NiNP surface, also increased the particle mobility which led to significant sintering from 5 nm to 20 nm after reduction at 500 °C.[30] Zacharaki *et al.* successfully deposited NiNPs on Al_2O_3 and effectively removed the ligands by thermal treatment with only slight sintering observed after reduction at 400 °C. Complete reduction was not achieved though, and this is necessary for hydrogenation catalysis.[14] More robust methods must therefore be developed to support well-defined colloidal nanoparticles and to maintain their dispersion if colloidal routes are to be considered a beneficial approach. To this end, nanoparticle confinement in porous matrices is considered a viable strategy. The stabilization of small (<2 nm) NiNPs through confinement in zeolite micropores has been investigated by Laprune *et al.*[41] and Goodarzi *et al.*[42] Brock and co-workers successfully encapsulated Ni_2P colloidal nanoparticles (d = 11 nm) in mesoporous silica to prevent their aggregation after ligand removal and catalyst activation.[43] Such strategies have been studied for supporting colloidal Pt and Pd nanoparticles,[44–47] as well as phosphorous-free colloidal NiNPs,[48–50] although these NiNP studies sought to support and stabilize particles larger than 20 nm. At present, no study has been able to produce well-defined colloidal NiNPs which vary in particle size and maintain their dispersion once supported and thermally activated (*i.e.* ligand removal and catalyst reduction), and are active in gas phase hydrogenation reactions. Ideally, such an approach would lead to catalysts that are tailored for a specific structure–sensitive reaction.

In this work, we report the preparation of mesoporous silica supported NiNPs prepared *via* the colloidal approach. By building a comprehensive set of colloidal NiNPs, we are able to isolate important factors controlling growth and nucleation using established colloidal nanoparticle growth theory. A two-step seed-mediated synthetic approach was developed, in which NiNP nucleation was induced with an external reducing agent under mild conditions. Particles were subsequently grown under thermal decomposition conditions (>200 °C) to obtain NiNPs between 3–8 nm using P-free ligands. Next, strategies to support the colloidal NiNPs and remove their ligands were investigated. Encapsulation of NiNPs in mesoporous silica produced active and stable hydrogenation catalysts. Moreover, encapsulation of colloidal NiNPs of different sizes ultimately led to a redistribution of the encapsulated Ni to yield catalysts with identical particle sizes and substantial catalytic activity. This approach demonstrates that colloidal NiNP growth can be effectively controlled using only mild capping agents, but that the support pore size becomes the controlling factor of the final NiNP size in encapsulated Ni@SiO_2 hydrogenation catalysts.

2 Experimental

2.1 Materials

Nickel acetylacetonate (anhydrous, 95%) was purchased from Strem, and oleylamine (OAm, technical, >70%), oleic acid (OAc, 90%), borane *tert*-butylamine complex (BTB, 97%), and cetrimonium bromide (CTAB, >99%) from Sigma Aldrich. Amorphous silica (Sipernat® 50 S, surface area 500 $m^2\ g^{-1}$) was purchased from Evonik. Hexane (99%), toluene (99.7%), $CHCl_3$ (99.9%, stab./amylene) were purchased from Biosolve, and tetraethyl orthosilicate (TEOS, >99%) from Merck. All chemicals were used as received without further purification.

2.2 Colloidal nanoparticle synthesis

Ni nanoparticles between 3–8 nm were synthesized using seed-mediated growth methods based on a combination of literature approaches.[19,38,39] To obtain the smallest particles (seeds), 257 mg $Ni(acac)_2$ (1 mmol), 15 mL oleylamine (OAm) and 0.32 mL oleic acid (OAc, 1 mmol) were added to a 250 mL two-neck round-bottomed flask equipped with a magnetic stirring bar. The mixture was brought under inert conditions by flushing with Ar and degassed at 110 °C for 30 min to removed oxygen and water. A green–blue solution was obtained. In a second flask, 0.44 g borane *tert*-butyl amine complex (BTB, 5 mmol) was dissolved in 2 mL OAm and degassed. The $Ni(acac)_2$ solution was cooled to 90 °C and the BTB solution was subsequently injected into the $Ni(acac)_2$ solution. The mixture went black within 30 s, signaling the reduction of the Ni^{2+} to metallic Ni. The synthesis continued for 1 h, after which the reaction was quenched by adding 17 mL toluene and cooled to room temperature. Nanoparticles were precipitated by adding acetone as an anti-solvent, followed by centrifugation (5000 rpm, 10 min). The supernatant was removed and the particles were washed by redispersing them in 5 mL toluene, followed by precipitation with 45 mL acetone and centrifugation. Particles were washed 3 times with the toluene/acetone mixture.

To obtain larger particles, the seeds were grown at elevated temperatures. After 1 h of the initial seed formation (as described above), the black solution was heated to 220 °C using a heating mantle. Additional $Ni(acac)_2$ (2–4 mmol) in equimolar OAc (2–4 mmol) was dissolved in octadecene (ODE, 10–20 mL) and was added dropwise to the round-bottomed flask using a Teflon cannula at a rate of *ca.* 0.5 mL min^{-1}. The particles were kept at 220 °C for an additional 1.5 h, after which the heating mantle was removed. Toluene was added to make a 1 : 1 solution with the colloidal NPs. Nanoparticles were precipitated, collected, and washed according to the procedure outlined above.

2.3 Supported colloidal nanoparticles

Ni(OAm)/SiO_2. The resulting colloidal NiNPs were subsequently supported on high surface area amorphous SiO_2 (Sipernat® 50 S, Degussa) with targeted metal loadings between 1–2 wt% Ni. NiNPs were dispersed in 5 mL of a non-polar organic solvent (*e.g.* toluene, $CHCl_3$). The NiNPs dispersion was added to a stirred suspension of 1 g SiO_2 in 15 mL of the same non-polar organic. The mixture was stirred for at least 12 h to ensure complete transfer of the NiNPs onto the support. The sample was then recovered by centrifugation, and washed 3 times by re-suspending the sample in the organic solvent through sonication, and subsequent centrifugation. The samples were dried overnight *in vacuo*. Samples synthesized are denoted by the solvent in which the colloidal NiNPs were suspended with Ni/SiO_2-h, Ni/SiO_2-t, and Ni/SiO_2-c denoting hexane, toluene, and chloroform suspended samples. In order to remove the organic ligands and to obtain the fully reduced metal catalyst, Ni/SiO_2 was reduced *in situ* in 10 vol% H_2 in He flow (100 mL min^{-1}) at 450–550 °C (2.5 °C min^{-1}, 6 h).

Encapsulation of NiNPs in SiO_2. Encapsulation of NiNPs in SiO_2 was carried out according to a literature procedure by Savithra *et al.*[43] Colloidal NiNPs (*ca.* 100 mg) were dispersed in 5 mL $CHCl_3$ and was slowly added to 20 mL aqueous CTAB solution (0.1 M) at room temperature. The transfer and stabilization of NiNPs from the organic to the aqueous phase was facilitated by heating the mixture to 75 °C and slowly evaporating the $CHCl_3$ for *ca.* 20 min to obtain a homogeneous black solution in contrast to the original cloudy brown mixture. The Ni/CTAB/H_2O mixture was cooled to 50 °C and diluted with 130 mL deionized water, to which 2 mL NaOH solution (1 M) was added. *In situ* hydrolysis of SiO_2 was performed by injecting 2.7 mL TEOS to the Ni/CTAB/H_2O solution dropwise over 5 min under stirring at 50 °C. The resulting gel-like mixture was stirred for 18 h. The product was isolated and centrifuge-washed 3 times with deionized water and 3 times with methanol. The product (Ni@SiO_2) was dried *in vacuo* overnight.

In order to remove the organic ligands (OAm/OAc) and templating/stabilizing agent (CTAB), Ni@SiO_2 was calcined in

20 vol% O_2 in N_2 mixture (50 mL min^{-1}) at 500 °C (1 °C min^{-1}, 10 h). The oxidized NiO@SiO_2 nanoparticles were reduced at 450–550 °C in 10 vol% H_2 in He flow (2.5 °C min^{-1}, 6 h).

2.4 Characterization

Transmission electron microscopy (TEM). Particle sizes of colloidal nanoparticles and supported nanoparticles were determined with TEM. Measurements were done on a FEI Tecnai 20 (type Sphera) transmission electron microscope operating at 200 kV. Typically, approximately 100 mg of the sample was crushed and suspended in pure $CHCl_3$, sonicated, and dispersed over a Cu grid with a holey carbon film.

High-angle annular dark-field scanning transmission electron microscopy (HAADF-STEM). The size and size distribution of encapsulated particles after reduction and CO_2 methanation were studied with HAADF-STEM. Images were acquired on the TU/e CryoTitan electron microscope (FEI, now Thermo Fischer Scientific). HAADF-STEM sample preparation involved sonication of the samples in pure ethanol (Biosolve, Extra dry, 99.9%) and applying a few droplets of the suspension to a 200 mesh Cu TEM grid with a holey carbon support film. Prior to imaging, the supported samples were left in an oven at 40 °C overnight to remove residual ethanol. STEM images were acquired using a probe convergence angle of 10 mrad, a dwell time of 2 μs and a camera length of 89 mm in combination with a Fischione HAADF detector.

X-ray diffraction. The crystal structure of the metal and crystallinity of the supports was studied using XRD. Samples were ground and pressed into sample holders for measurements. XRD patterns were recorded on a Bruker D2 Phaser diffractometer using Cu Kα radiation with a wavelength of 1.54 Å. The 2θ angles were measured with a step size of 0.02° at 1.0 s per step. For Ni@SiO_2, additional small angle measurements were performed between 0.1–1°, with a step size of 0.0015° at 0.25 s per step.

N_2 physisorption. Textural properties of the SiO_2-based systems were performed at −186 °C on a Micromeritics TriStar II 3020. The sample (*ca.* 150 mg) was degassed at 120 °C for 12 h prior to sorption measurements. Surface areas were computed using the Brunauer–Emmett–Teller (BET) method, and pore size distributions and total pore volumes were calculated by the Barrett–Joyner–Halenda (BJH) method using the desorption branch of the isotherm.

Temperature programmed reduction (TPR). The reducibility of encapsulated nanoparticles was studied with TPR in a Micromeritics AutoChem II. Typically, 50–100 mg of sample was transferred to a quartz U-tube. The sample was dried at 130 °C for 1 h under He. TPR was performed by linearly heating the sample to 800 °C in a flow of 4 vol% H_2 in He at 50 mL min^{-1}. The gas consumption was measured by a TCD and calibrated using a CuO/SiO_2 reference catalyst.

H_2 chemisorption. The available metal sites for encapsulated nanoparticles were probed by H_2 chemisorption using a Micromeritics ASAP 2020. Typically, 100 mg catalyst was loaded into a quartz U-tube reactor. Prior to H_2 chemisorption, the sample was reduced at 600 °C by heating to this temperature at a rate of 5 °C min^{-1}, followed by an isothermal dwell of 4 h. After evacuation at 620 °C to remove all hydrogen species, H_2 chemisorption was carried out at 35 °C.

X-ray photoelectron spectroscopy (XPS). Surface Ni oxidation state for colloidal NiNPs was studied with XPS. Finely crushed samples were placed on double-sided carbon tape and analyzed using a K-Alpha XPS apparatus (Thermo Scientific). Spectra were obtained using an Al anode (Al Kα = 1486.68 eV) with 50 scans in the Ni 2p region. Depth profiling was performed to study encapsulated NiNPs after reduction at 600 °C and passivation in 1 vol% O_2 in He (6 h). Finely crushed samples were placed on double-sided carbon tape and were studied after exposure to an Ar^+ ion gun at 3.0 keV for 0–300 s. Ni/Si ratios were used to estimate the elemental composition. All spectra were analyzed with CasaXPS, charge corrected against the C 1s binding energy of adventitious carbon at 284.8 eV, and were fitted using a Shirley background.

2.5 Catalytic activity measurements

The catalytic activity of the prepared samples for gas-phase hydrogenation reactions was performed in a 10-channel high-throughput flow reactor. Prepared samples were pelletized at a pressure of 300 MPa and sieved to a 75–125 μm fraction. Approximately 50 mg catalyst (75–125 μm) was diluted with 150 mg SiC and loaded into a quartz reactor tube with an internal diameter of 0.4 cm. Quartz wool was used before and after the catalyst bed. Effluent products were analyzed by online gas chromatography (Interscience CompactGC) equipped with Restek Rt-Q-Bond and Rt-Msieve 5 Å (TCD), Restek Rt-U-Bond and Rt-Q-Bond (TCD), and Restek Rtx-1 (FID) columns.

Benzene hydrogenation. Supported colloidal Ni catalysts were pretreated in a 100 mL min^{-1} flow of 10 vol% H_2 in He at 450–550 °C (ramp rate 2.5 °C min^{-1}, dwell 6 h) and cooled to the 70 °C, which is the starting temperature of the temperature programmed reaction. A gas mixture of 1.5 mL min^{-1} C_6H_6, 30 mL min^{-1} H_2, and 68.5 mL min^{-1} He was prepared using a controlled evaporation mixer (CEM) kept at 50 °C. First, a 7.5 vol% C_6H_6 mixture was prepared by evaporating 3.2 g h^{-1} C_6H_6 in a He flow of 185 mL min^{-1}. The resulting C_6H_6 gas mixture was diluted with 500 mL min^{-1} He and 300 mL min^{-1} H_2, and subsequently separated over 10 quartz reactors. The weight hourly space velocity (WHSV) was 5.8 g g_{cat}^{-1} h^{-1}. Rates were normalized to the total Ni loading.

CO_2 methanation. Encapsulated Ni@SiO_2 catalysts were studied in CO_2 methanation using the same high-throughput setup as described above. CO_2 methanation was performed at atmospheric pressure. Prior to catalytic testing the samples were reduced at 600 °C for 3 h in 10 vol% H_2 in He at a flow rate of 50 mL min^{-1}. The catalytic performance was tested with a supply of 3 vol% CO_2, 12 vol% H_2, and 85 vol% He at

50 mL min^{-1}. Steady-state CO_2 conversion was measured between 200 and 400 °C. The stability of the catalyst is tested at 350 °C with the same feed composition. The CO_2 conversion (X_{CO_2}), and CH_4 (S_{CH_4}) and CO (S_{CO}) selectivities are calculated as:

$$X_{CO_2} = \frac{[CH_4]+[CO]}{[CO_2]+[CH_4]+[CO]} \quad (1)$$

$$S_{CH_4} = \frac{[CH_4]}{[CH_4]+[CO]} \quad (2)$$

$$S_{CO} = \frac{[CO]}{[CH_4]+[CO]} \quad (3)$$

3 Results and discussion

3.1 Ni particle size control

The general procedures for the colloidal synthesis of Ni nanoparticles employed here are summarized in Fig. 1 with the main results summarized in Table 1. Representative TEM images for obtained NiNPs are shown in Fig. 2. Benchmark procedure 1 involved the synthesis of the colloidal NiNPs through thermal decomposition of $Ni(acac)_2$ in the presence of an equimolar amount of oleic acid (OAc) and excess oleylamine (OAm) at 220 °C. OAc was used as a co-surfactant to efficiently solvate Ni^{2+} in the non-polar organic solution. This procedure resulted in polydisperse NiNPs with an average particle size of 53 nm (Fig. 2a), despite the large excess of 46 equivalent of OAm. The results are consistent with earlier reports by Zhang *et al.*[17] and Carenco *et al.*[19] Previously, the large sizes and broad size distribution of the NPs were attributed to the rapid reduction of Ni^{2+} to Ni(0) by OAm, leading to a burst of Ni(0) species which could not be effectively stabilized by OAm and therefore aggregate into polydisperse particles.[19]

To obtain smaller particles with a narrower size distribution, lower-temperature procedures (90 °C) with an external reducing agent were applied (procedures 2–4, Fig. 1, Table 1).[38] Borane *tert*-butylamine (BTB) was dissolved in OAm and injected into the $Ni(acac)_2$/OAc/OAm solution, turning the mixture black almost instantly (procedure 2). The rapid injection of the external reducing agent leads to a supersaturated solution during which particle nucleation occurs. It is vital that this step is carried out rapidly to achieve homogeneous nucleation and obtain colloidal NPs with a narrow particle size distribution. TEM images confirm that nanoparticles of 4.4 nm were obtained for BTB/Ni = 5 after 1 h growth at 90 °C (Fig. 2b). After precipitating out the NiNPs using a toluene/acetone mixture, the remaining supernatant still appeared slightly green, suggesting that not all the Ni^{2+} had been reduced.

To obtain larger particles, the nanoparticles were preformed at 90 °C and rapidly heated to 220 °C. Additional $Ni(acac)_2$ (2 or 4 mmol) dissolved in OAc (2 or 4 mmol, respectively) and ODE (10 or 20 mmol, respectively) was added dropwise to the colloidal dispersion (procedures 3 and 4 respectively, Fig. 1, Table 1). NiNPs of 6.3 nm and 7.9 nm were obtained in this way by the addition of 2 mmol and 4 mmol $Ni(acac)_2$ to the initial suspension at 220 °C. The Ni^{2+} concentration and the rate of addition were kept constant during the different procedures.

Structural properties of as-synthesized colloidal NiNPs were studied by XRD (Fig. 3). NiNPs synthesized *via* the BTB reduction pathway (procedures 2–4) did not exhibit crystalline phases in XRD which we attribute to the small particle size.[51,52] Low-intensity contributions between 40–45° are likely from amorphous carbon deposits. In contrast, the XRD pattern of NiNPs synthesized by direct thermal decomposition of $Ni(acac)_2$ showed sharp diffraction peaks at 39.1°, 41.6°, 44.6°, 58.4°, 71.0°, and 78.0° correspond to the (100), (002), (101), (102), (110), and (103) crystal planes of hcp-Ni_3C

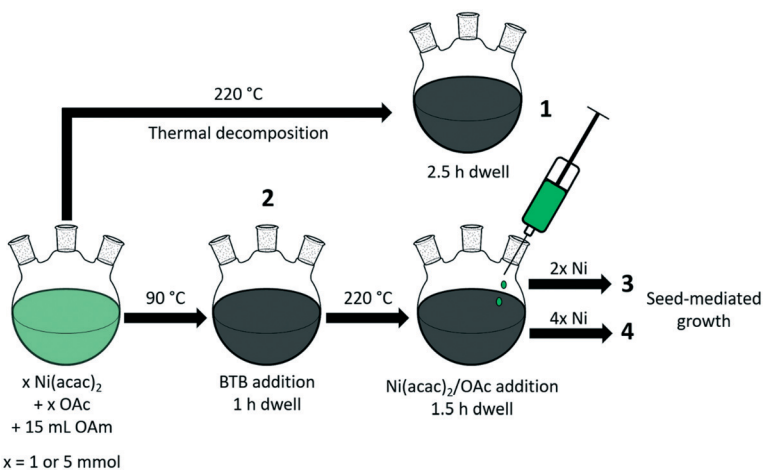

Fig. 1 Schematic illustration of Ni nanoparticle synthesis procedures 1–4.

Table 1 Summary of conditions for Ni nanoparticle synthesis and obtained particle sizes

Procedure	Initial $Ni(acac)_2$ (mmol)	BTB/Ni	T (°C)	$Ni(acac)_2$ added (mmol)	d (nm)	Fraction Ni^{0b} (%)
1	5	n/a	220	0	53 (± 14)	47
2	1	5	90	0	4.4 (± 0.5)	22
3[a]	1	5	90, 220	2	6.3 (± 1.0)	12
4[a]	1	5	90, 220	4	7.9 (± 1.5)	39

[a] BTB injection at 90 °C, $Ni(acac)_2$ addition at 220 °C. [b] Air exposed. Surface fraction determined by XPS.

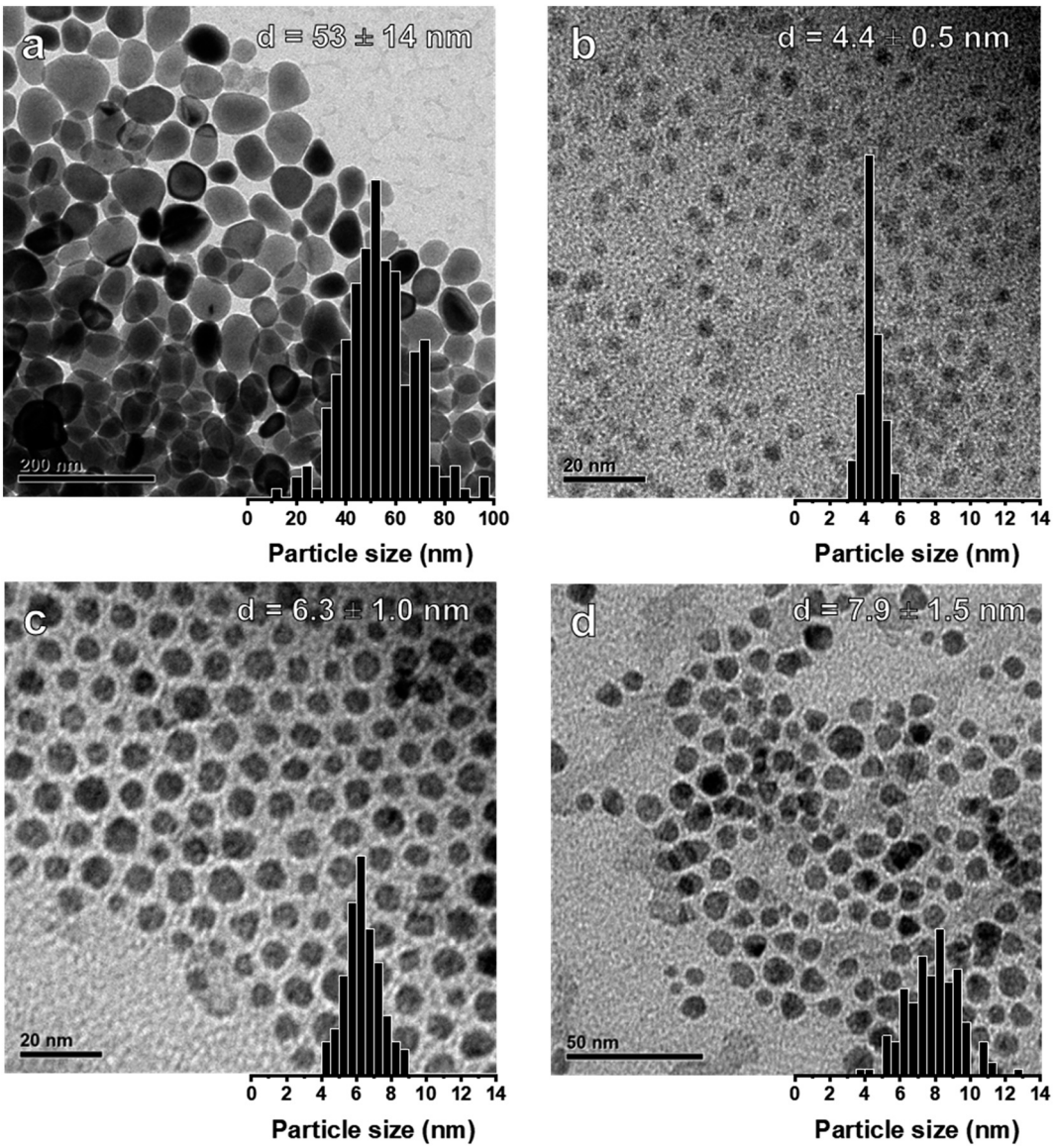

Fig. 2 (a) TEM image and distribution of colloidal NiNPs prepared by thermal decomposition of $Ni(acac)_2$ in OAm at 220 °C (procedure 1). Colloidal NiNPs prepared using seed-mediated growth methods: (b) initial particles produced with BTB/Ni = 5 at 90 °C (procedure 2). By increasing the temperature to 220 °C, particles were grown by the dropwise addition of (c) 2 equivalents (procedure 3) or (d) 4 equivalents (procedure 4) $Ni(acac)_2$ in an OAc/ODE solution.

(JCPDS no. 04-0853). The hexagonal lattice constants of a = 2.65 Å and c = 4.35 Å match those reported in literature for hcp-Ni_3C.[53–55] Colloidal routes providing Ni_3C nanoparticles have been reported before during synthesis carried out above 200 °C, with carbon contaminations of the organic surfactants yielding the carbide phase.[54–57] However, due to the nearly similar lattice parameters of hcp-Ni_3C and metastable hcp-Ni, we cannot only rely on XRD to discern between these

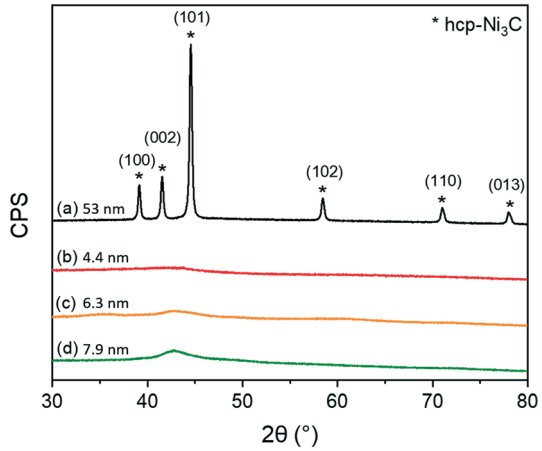

Fig. 3 XRD patterns for the colloidal NiNPs synthesized by (a) thermal decomposition at 220 °C (procedure 1), (b) BTB addition at 90 °C to give the smallest NiNPs (procedure 2). Seed-mediated approaches were ramped to 220 °C and either (c) 2 equivalents (procedure 3) or (d) 4 equivalents of $Ni(acac)_2$ (procedure 4) was added dropwise.

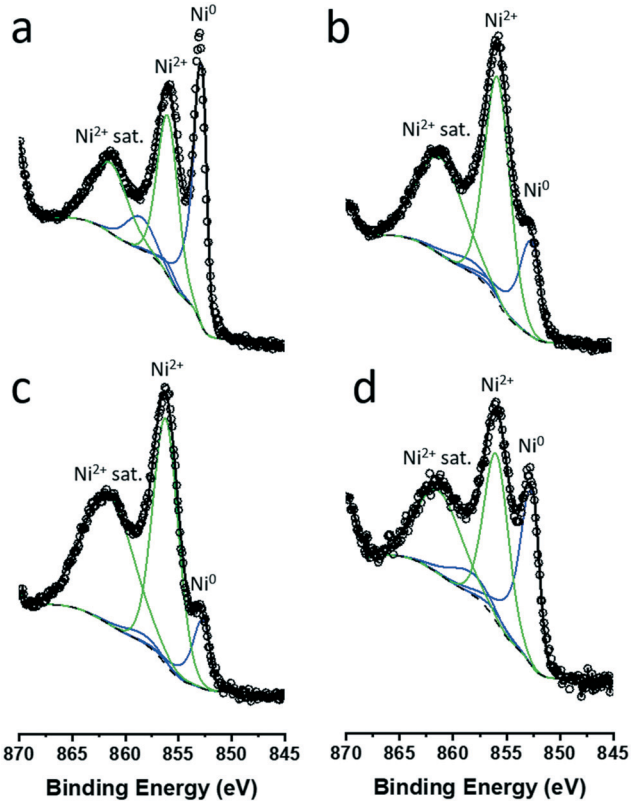

Fig. 4 Fitted XP spectra in the Ni $2p_{3/2}$ region of colloidal NiNPs synthesized by (a) thermal decomposition at 220 °C (procedure 1, d = 53 nm), and (b) BTB addition at 90 °C (procedure 2, d = 4.4 nm). XP spectra of NiNPs obtained synthesized by seed formation at 90 °C and particle growth at 220 °C by (c) 2 eq. Ni addition (procedure 3, d = 6.3 nm), and (d) 4 eq. Ni addition (procedure 4, d = 7.9 nm). Open circles represent raw data, and metallic Ni^0 (blue) and Ni^{2+} (green) contributions were fitted.

two crystal phases.[53] The carbide phase was confirmed by XPS measurements of the C 1s region (see ESI†). By etching the NiNP surface with Ar^+ ions, a peak positioned at 283.5 eV emerged, which could be attributed to the Ni–C bond.[54] This phase is metastable and decomposes into fcc-Ni in reducing atmospheres above 300 °C.[58,59] XPS measurements of the C 1s region after Ar^+ etching did not reveal a Ni–C phase for these smaller NiNPs (see ESI†).

The nature of the particles was studied further with XPS. XP spectra of colloidal NiNPs after exposure to air were obtained in the Ni $2p_{3/2}$ region (Fig. 4). Despite the absence of oxidic Ni phases in XRD, we observed both metallic Ni^0 (BE = 852.8 eV) as well as oxidized Ni^{2+} (main peak BE = 856.0 eV, satellite peak BE = 861.5 eV) on all NiNPs, confirming that the NiNPs readily passivated in air. Larger colloidal NiNPs appeared to be more resistant to passivation as evidenced by a higher Ni^0 fraction (Table 1).

Interestingly, our results demonstrate that OAm is an effective capping agent at temperatures at which $Ni(acac)_2$ decomposes (>200 °C).[60] This result contrasts earlier findings by Carenco *et al.*, who determined OAm to be a weak capping agent under thermal decomposition conditions, leading to large, polydispersed nanoparticles.[19] Based on our data, we speculate that OAm is an adequate capping agent but a poor reducing agent, resulting in an ineffective nucleation and slow growth. The theory of colloidal nanoparticle growth has been reviewed in great detail elsewhere.[1,3,15,61,62] In the absence of an external reducing agent, atomic Ni monomer formation is kinetically limited during the temperature ramp to 220 °C. Therefore, once (local) supersaturation is achieved, Ni seeds are formed and the monomer concentration decreases below the threshold concentration for nucleation. However, due to the slow $Ni(acac)_2$ decomposition, relatively few seeds are formed when compared to an approach employing an external reducing agent. The low seed concentration leads to large particles. Moreover, as decomposition kinetics increase at higher temperature, the rate of monomer formation is also increased. If the monomer concentration exceeds the threshold concentration required for supersaturation, nucleation will occur resulting in the formation of new seeds. The formation of new seeds during the growth of existing seeds is the main cause of the broad particle size distribution. With our seed-mediated approach, we obtain a rapid increase in monomer concentration at low temperatures which leads to homogeneous nucleation. These particles maintain their narrow size distribution upon increasing the temperature to 220 °C. Further addition of $Ni(acac)_2$ under decomposition conditions maintains a low monomer concentration and grows the existing particles rather than nucleating new ones. Overall this approach allows a better control of NiNP synthesis. In contrast, addition of $Ni(acac)_2$ at 90 °C did not result in the formation of larger particles, but in a higher yield of NiNP (see the ESI†), confirming that the low-temperature seed formation must be combined with the high-temperature particle growth to obtain larger particles. To the best of our knowledge, this is the first report of seed-mediated NiNPs able to control nanoparticle growth

below 10 nm, with earlier studies reporting particles larger than 25 nm.[17]

3.2 Colloidal Ni/SiO_2

Initially, two approaches were explored to support pre-synthesized colloidal NiNPs: direct deposition on SiO_2 and encapsulation in SiO_2. An initial set of 3 catalyst samples were prepared *via* direct deposition by contacting the colloidal NiNPs with a commercial SiO_2 support. The NiNPs were either dispersed in hexane (Ni/SiO_2-h), toluene (Ni/SiO_2-t), or chloroform (Ni/SiO_2-c). Alternatively, colloidal NiNPs were encapsulated by first dispersing the particles in $CHCl_3$, adding the dispersion into a CTAB solution. $CHCl_3$ was removed by evaporation at 75 °C to yield CTAB-stabilized, OAm capped colloidal NiNPs in H_2O.[43] This double-micelle approach stabilizes the hydrophobic colloidal nanoparticles in aqueous media. Particles were encapsulated in SiO_2 by adding the molecular silicon precursor TEOS under basic conditions. The hydrolysis of TEOS and condensation of silica was allowed to proceed for at least 12 h. The sample was washed extensively and calcined at 500 °C to remove all templating agents. For all samples, low Ni loadings (*ca.* 1–2 wt%) were used to minimize particle aggregation during ligand removal and catalyst activation, both achieved by reduction in 10 vol% H_2 in He at 450 °C. All samples had initial colloidal NiNP sizes around 3.5 nm (Table 2), achieved by following procedure 2 and allowing only 5 min growth time. These particles were only used in this initial screening study.

TEM images obtained for directly deposited NiNPs after reductive treatment at 450 °C are presented in Fig. 5a–c. The images highlight the differences in the aggregation of the Ni phase. A weak interaction between the commercial SiO_2 and colloidal NiNPs led to ineffective anchoring of the NiNPs, as evident from the sintering after reduction. In contrast, encapsulated nanoparticles (Fig. 5d) retained their initial particle size (3.5 ± 0.5 nm), even after reduction at 550 °C.

To verify the potential of these samples for catalysis, they were employed in the gas-phase benzene hydrogenation to cyclohexane. This reaction, regarded as structure-insensitive, probes the hydrogenation properties of the supported colloidal nanoparticles. Fig. 6 shows turnover frequencies (TOFs) measured at 100 °C normalized to the total Ni content for the supported and encapsulated NiNPs. Hexane deposited NPs were not studied due to the significant sintering observed by TEM. After reduction at 450 °C, the encapsulated NiNPs were more active than the directly deposited particles.

Table 2 ICP determined Ni loadings and TEM determined initial particle sizes (prior to deposition/encapsulation). Further characterization is presented in the ESI

Sample	Solvent	wt% Ni	d_1 (±), nm
Ni/SiO_2-h	Hexane	2.1	3.4 (0.5)
Ni/SiO_2-t	Toluene	0.7	3.7 (0.7)
Ni/SiO_2-c	$CHCl_3$	1.2	3.7 (0.7)
$Ni@SiO_2$	$CHCl_3/H_2O$	1.2	3.7 (0.7)

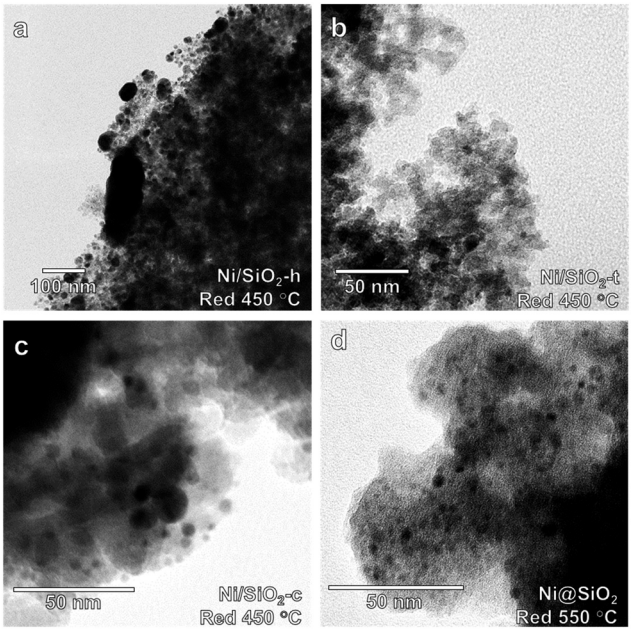

Fig. 5 TEM micrographs of (a) hexane, (b) toluene, and (c) chloroform suspended NiNPs deposited on amorphous SiO_2 after reduction at 450 °C. (d) NiNPs encapsulated in mesoporous SiO_2 after reduction at 550 °C showing an average particle size of 3.5 nm.

Pre-calcination of directly deposited NiNPs did not improve the catalytic performance of these materials (ESI†). Clearly, encapsulation of NiNPs yielded superior performing catalysts compared to direct deposition, showing significantly higher hydrogenation activity after catalysts were reduced at 450 °C. We also found that reduction at 550 °C led to even higher activity for the encapsulated NiNPs, whereas this treatment strongly decreased the performance of the deposited NiNP catalyst. The high activity after reduction at 550 °C should be due to a higher reduction degree, whilst this positive effect is suppressed by sintering for the deposited NiNP catalyst. Although sintering was observed for Ni/SiO_2-t, this sample surprisingly was not active at all. Based on these results, we conclude that supporting the NiNPs by encapsulation is the most viable approach to study particle size effects in supported Ni

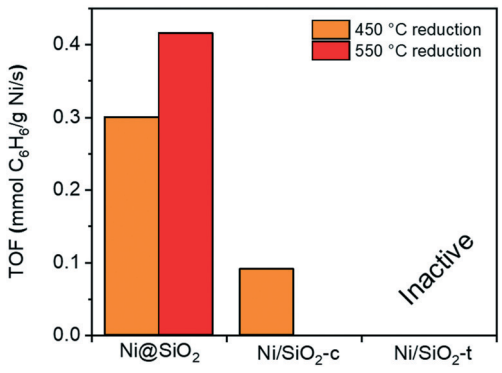

Fig. 6 Gas-phase benzene hydrogenation TOFs at 100 °C over encapsulated $Ni@SiO_2$, Ni/SiO_2-c and Ni/SiO_2-t after reduction at 450 °C and 550 °C.

catalysts and proceeded to investigate this synthetic route in greater detail.

3.3 Encapsulation of NiNPs in mesoporous SiO_2

Having optimized both NiNP synthesis and NiNP supporting techniques, a set of encapsulated Ni(*x*)@SiO_2 catalysts was prepared in which *x* denotes the original NiNP size. Procedures 2, 3, and 4 were used to synthesize the NiNPs of 4.4 nm, 6.8 nm, and 7.2 nm respectively. The new set of colloidal nanoparticles were similar in size compared with those obtained in the earlier synthesis optimization work, highlighting the method's reproducibility. Particles of 5.0 nm were obtained by rapid heating of the initial BTB/Ni solution from 90 °C to 220 °C without injecting additional $Ni(acac)_2$ under thermal decomposition conditions, indicating that unreduced Ni^{2+} at 90 °C may still be reduced at 220 °C, growing the existing NiNPs from *ca.* 4.4 to 5.0 nm. After extensive washing and vacuum drying, approximately 200 mg colloidal NiNPs was supported *via* encapsulation. Ligand and templating agents were removed by slow calcination at 500 °C (10 h, 1 °C min^{-1}), as determined by TGA analysis (see ESI†). Ni content and physical characterization of calcined materials are summarized in Table 3. BET surface areas were determined by N_2 physisorption (see ESI†) and were high for all catalysts, ranging between about 890–980 $m^2\ g^{-1}$.

Further characterization with XRD (Fig. 7) showed that the catalysts were largely amorphous after calcination. The broad reflection around 22° is characteristic of amorphous silica. NiO reflections were only observed for the higher loaded Ni(7.2)@SiO_2 and to a lesser extent Ni(5.0)@SiO_2 catalysts. Sharp reflections from (200) and (220) planes were observed around 43.7° and 64.0°, respectively, indicating the formation of large NiO crystallites (JCPDS no. 47-1049), which we verified with HAADF-STEM (ESI†). Moreover, very weak and broad contributions centered around 35.2° (envelope of two reflection peaks) and 61.0° are indicative of a Ni-silicate phase (JCPDS no. 49-1859).[63,64] This was a first indicator that the nanoparticle-like structure of NiNPs is lost during calcination. Low-angle XRD measurements (Fig. 7b) confirmed the presence of MCM-41 like mesoporous structures in all catalysts. The average mesopore size was calculated from the *d*-spacing derived from the position of the (100) reflection and ranged from 4.4 nm for Ni(4.4)@SiO_2, to 5.4 nm for Ni(7.2)@SiO_2 (Table 3).

Crucial to the catalytic activity of Ni-based hydrogenation catalysts is the reducibility of Ni and the availability of metallic Ni active sites. Fig. 8 shows the TPR profiles of encapsulated nanoparticles after calcination. All catalysts exhibit a maximum reduction temperature between 600–650 °C, which is characteristic of Ni strongly interacting with the support. Shoulders around 450 °C can be attributed to the reduction of NiO weakly interacting with SiO_2. Moreover, the total hydrogen consumption scales with the total Ni content, whilst the TPR profiles are composed of similar features.

Further verification that the Ni was encapsulated after reduction was achieved with XPS depth-profiling. Fig. 9 shows surface Ni/Si molar ratios upon successive Ar^+ etching. Samples were first reduced *ex situ* at 600 °C in 10 vol% H_2 in He and passivated in 1 vol% O_2. After Ar^+ etching for 60 s, all samples exhibited higher Ni/Si ratios, which confirmed an increase in the Ni content below the support surface. This trend continued with every etching dose, although samples with lower overall Ni content saw the Ni/Si ratios plateau after 2–3 doses.

3.4 The effect of encapsulation on final particle sizes

The particle sizes in Ni(*x*)@SiO_2 catalysts reduced at 600 °C (4 h, 5 °C min^{-1}) were determined by both HAADF-STEM and H_2 chemisorption (Table 3). To our surprise, HAADF-STEM images (Fig. 10) revealed that after reduction, all catalysts possessed a nearly identical particle size of around 4.5 nm with a narrow particle size distribution. As low-angle XRD showed that the pore sizes of the silica support were always in the 4.4–5.4 nm range, we infer that the silica pore size determines the final size of the reduced Ni particles. In fact, HAADF-STEM images of calcined Ni(7.2)@SiO_2 revealed the formation of nest-like NiO species (see ESI†), similar to those observed in studies investigating nickel phyllosilicate reduction.[63] Park *et al.* observed nickel phyllosilicate after calcination of silica-coated nanoparticles capped by OAm/TOP in the absence of templating agents.[64] We speculate that the nest-like NiO species are formed throughout the mesoporous network and decompose into encapsulated nanoparticles during reduction, with the pore size restricting the maximum Ni particle size. The robustness of the mesoporous network therefore hinders the preparation of catalysts with larger Ni particles. Although silica growth optimization was beyond the scope of this study, strategies to obtain catalysts with larger

Table 3 Physico-chemical properties of encapsulated NiNPs

Sample	Ni wt%[a]	BET ($m^2\ g^{-1}$)	V_{tot} ($cm^3\ g^{-1}$)	Pore size[b] (nm)	H_2 chem. (mmol g^{-1})	Accessible metallic Ni (%)	*d* (nm)	
							H_2 chem.	HAADF-STEM[c]
Ni(4.4)	2.4	979	1.46	4.4	0.019	9.1	11.1	4.3 (± 0.6)
Ni(5.0)	4.8	983	1.74	4.9	0.052	12.9	7.9	4.6 (± 0.6)
Ni(6.8)	3.7	964	2.15	4.7	0.036	11.4	8.9	4.7 (± 0.7)
Ni(7.2)	8.6	891	1.18	5.4	0.087	11.8	8.6	4.6 (± 0.6)

[a] Determined with ICP-OES after calcination at 500 °C. [b] Determined from *d*-spacing using the position of the SiO_2 (100) diffraction obtained from low-angle XRD measurements. [c] Samples were reduced at 600 °C (10 vol% H_2) and passivated at RT (1 vol% O_2, 6 h).

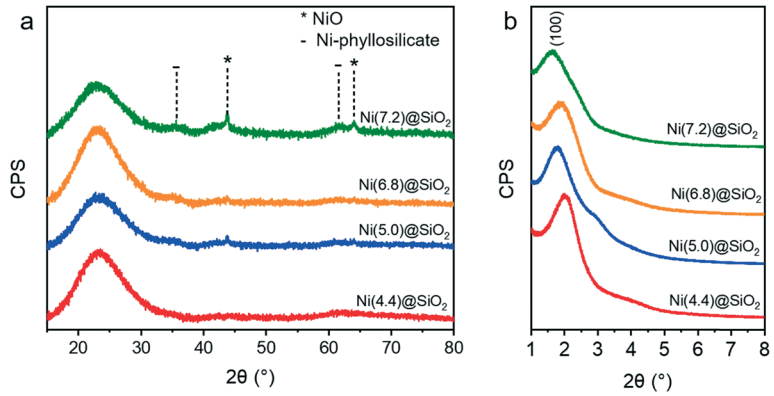

Fig. 7 (a) Wide angle XRD patterns of encapsulated NiNPs after calcination at 500 °C (10 h, 1 °C min^{-1}). (b) Small-angle XRD confirming the presence of MCM-41 like mesopores for all catalysts.

particles might require alternative templating agents to obtain larger mesopores. Particle sizes calculated from H_2 chemisorption measurements assume a $H/Ni_{surface}$ stoichiometry of unity, and that accessible metallic Ni is equal to the dispersion. Accessible metallic Ni is defined as the percentage of Ni chemisorbing H_2 relative to the total amount of Ni. This differs from dispersion because dispersion assumes that all Ni particles are accessible. Interestingly, comparing the particle sizes derived from H_2 chemisorption (*i.e.*, assuming accessible metallic Ni equals dispersion) with those obtained from HAADF-STEM, we see that H_2 chemisorption underestimates the dispersion, which suggests that a fraction of the NiNPs are completely encapsulated by SiO_2. This part of the Ni phase should be inactive in catalysis.

3.5 Catalytic performance in CO_2 methanation: activity and stability

The catalytic activity of Ni(*x*)@SiO_2 catalysts for CO_2 methanation was examined between 200–400 °C in a high-throughput fixed-bed reactor at atmospheric pressure and using a stoichiometric H_2/CO_2 ratio of 4. Catalysts were reduced *in situ* at 600 °C prior to exposure to the reaction mixture. The stability of these materials was also part of our investigations, studying the conversion of the same materials at 350 °C for 70 h.

All catalysts were active within the studied temperature range, showing a typical Arrhenius behavior of the conversion at low temperature and deviation from this trend due to the approach to equilibrium at higher temperature (Fig. 11a). No hydrocarbons other than CH_4 were detected. Turnover frequencies (TOFs) normalized to surface Ni content were calculated under differential conditions (<10% conversion) at 250 °C (Table 4). No CO formation was observed under these conditions (Fig. 11b). The TOFs revealed that there was no significant difference in catalytic activity, which can be expected as the encapsulated catalysts are almost identical apart from their Ni content. These TOFs are comparable to those reported in literature for Ni/SiO_2 systems.[65,66] Identical apparent activation energies were also determined for encapsulated catalysts (~75 kJ mol^{-1}) which is in line with literature values.[65–68] These results confirm that there are no adverse effects on the Ni activity by encapsulating the particles in mesoporous silica, and that the catalysts were free from mass transfer limitations.

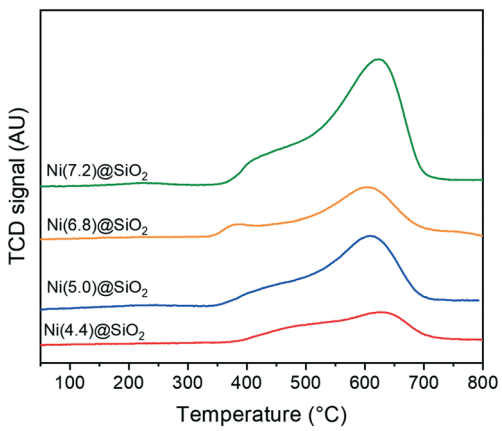

Fig. 8 H_2-TPR profiles of Ni(*x*)@SiO_2 catalysts.

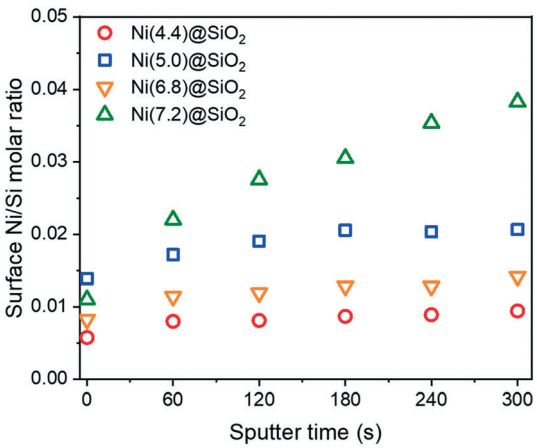

Fig. 9 XPS derived surface Ni/Si molar ratios of encapsulated Ni(*x*)@SiO_2 samples after calcination at 500 °C and reduction at 600 °C. Samples were exposed to 5 doses of Ar sputtering to obtain a depth profile.

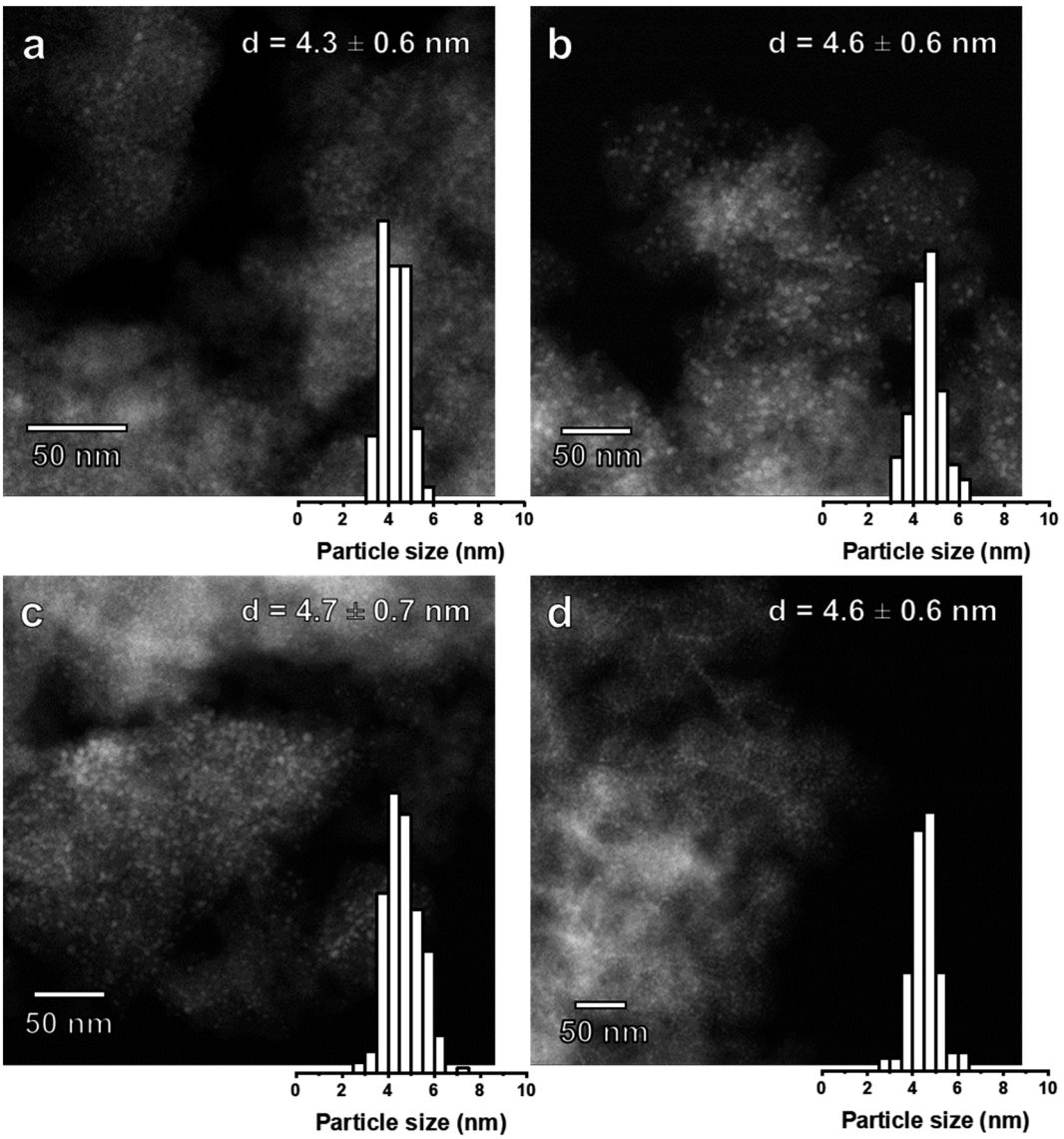

Fig. 10 HAADF-STEM images and particle size distribution of (a) Ni(4.4)@SiO_2 (b) Ni(5.0)@SiO_2 (c) Ni(6.8)@SiO_2 and (d) Ni(7.2)@SiO_2 catalysts after reduction at 600 °C (50 nm scale bar).

Similar conversion trends were observed during the stability study at 350 °C (Fig. 11c) in which all catalysts were found to be stable for 70 h. Catalysts with a lower Ni content exhibited higher CO selectivities. The catalyst with the lowest Ni content, *i.e.* Ni(4.4)@SiO_2, had a CO selectivity of 43–47% during the entire study. In contrast the highest loaded catalyst, Ni(7.2)@SiO_2, had a CO selectivity below 10% throughout the stability test (Fig. 11d). The slight increase in CO selectivity for Ni(4.4)@SiO_2, Ni(5.0)@SiO_2, and Ni(6.8)@SiO_2 catalysts during the stability test may indicate that some of the particles on the external SiO_2 surface sintered under reaction conditions. Earlier studies have shown that larger Ni particles have a higher selectivity towards CO.[69]

To verify whether Ni dispersion changed during the catalytic reaction, spent catalysts were analyzed with HAADF-STEM. Fig. 12 shows HAADF-STEM images of Ni(4.4)@SiO_2 (2.4 wt% Ni) and Ni(7.2)@SiO_2 (8.6 wt% Ni), *i.e.* the catalysts at the extreme ends of the initial colloidal particle size and metal loadings, after 70 h CO_2 methanation. For Ni(4.4)@SiO_2, evidence of particle aggregation was found, although there were clearly also particles that were identical to the initial particle size. This suggests that some particles were not encapsulated and their mobility under reaction conditions led to some sintering. In contrast, encapsulated NiNPs (Fig. 12a, circled) retained their original particle size. This was also observed for Ni(7.2)@SiO_2 (Fig. 12b) and the remaining Ni(x)@SiO_2 catalysts (see ESI†), which had a higher Ni loading and showed no evidence of particle aggregation. Moreover, we observed significant areas in Ni(4.4)@SiO_2 that did not contain NiNPs. We anticipate therefore that with an encapsulation approach in which SiO_2

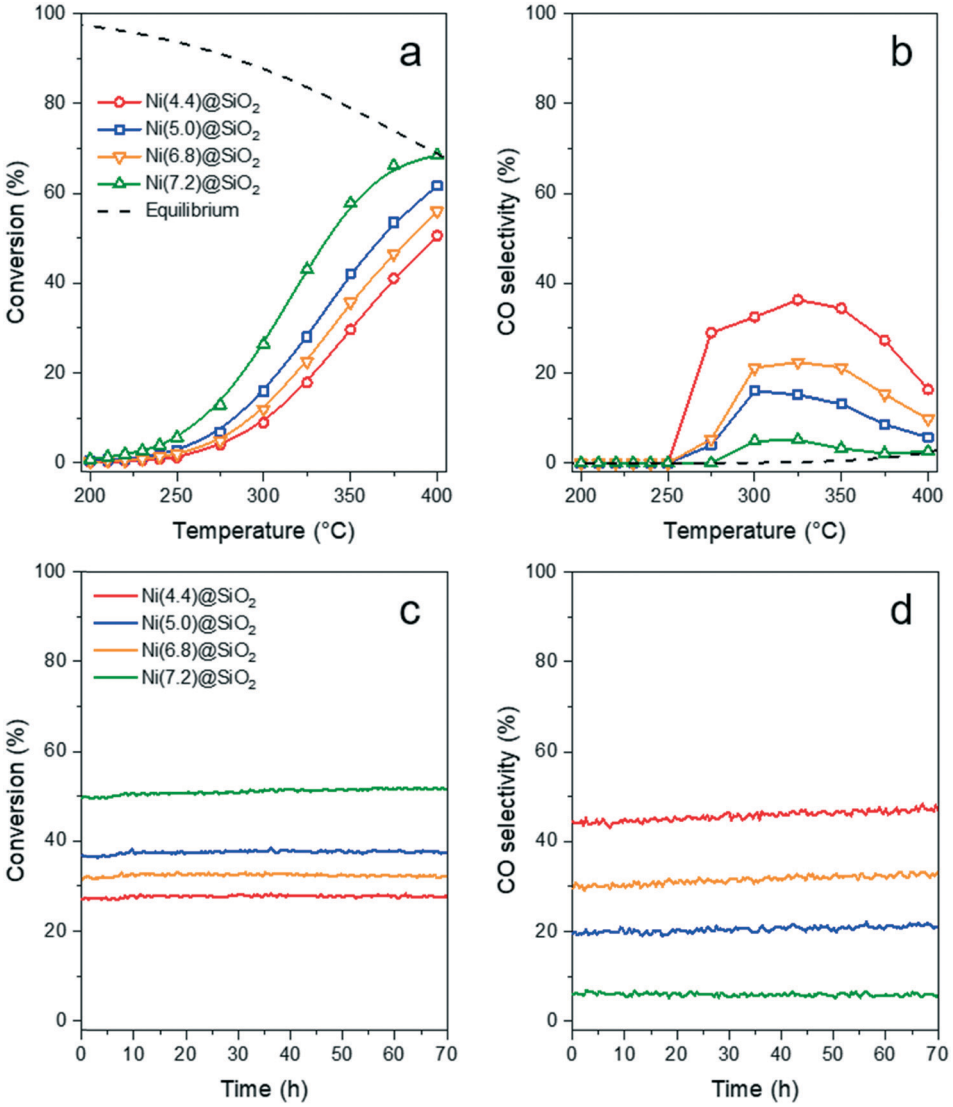

Fig. 11 CO_2 methanation (H_2/CO_2 = 4, 50 mL min^{-1}) over Ni(*x*)@SiO_2 showing the (a) CO_2 conversion and (b) CO selectivity between 200–400 °C. Catalyst stability was studied at 350 °C and (c) CO_2 conversion and (d) CO selectivity remained stable during 70 h.

is grown around the NiNPs, Ni catalysts with loadings significantly higher than 8 wt% should be attainable without nanoparticle sintering. Such an approach appears more promising than methods like impregnation or chemical vapor deposition in mesoporous silica or other zeotype materials, in which the possibility of Ni deposition outside of mesopores and cavities (*i.e.*, on the external crystal surface) and Ni aggregation are more difficult to control.[42,70,71] Across all samples, particle sizes remained essentially unchanged, with sintering attributed to unencapsulated nanoparticles.

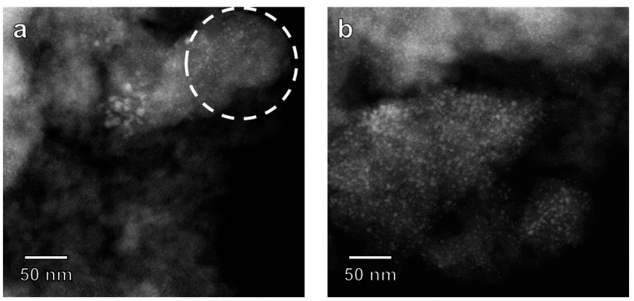

Fig. 12 HAADF-STEM images of (a) Ni(4.4)@SiO_2 and (b) Ni(7.2)@SiO_2 catalysts after exposure to CO_2 methanation conditions.

4 Conclusions

Colloidal NiNPs were successfully synthesized and grown using a seed-mediated approach to give particle sizes between 3–8 nm. To the best of our knowledge, this is the first seed-mediated approach reported for colloidal Ni nanoparticle synthesis that controls particle sizes below 10 nm without employing P-ligands. In addition, these colloidal NiNPs were encapsulated in mesoporous SiO_2 to yield active and highly stable methanation catalysts. Despite gaining control over

Table 4 Kinetic results for Ni(*x*)@SiO_2 catalysts for CO_2 methanation at 250 °C

Sample	Conversion (%)	CH_4 selectivity (%)	TOFs (10^{-3} mol CH_4 per mol surface Ni per s)	E_{act}^{app} (kJ mol^{-1})
Ni(4.4)@SiO_2	1.3	100	7.0 (± 0.4)	75
Ni(5.0)@SiO_2	2.9	100	5.7 (± 0.02)	75
Ni(6.8)@SiO_2	2.0	100	5.7 (± 0.09)	74
Ni(7.2)@SiO_2	5.7	100	6.7 (± 0.03)	77

the colloidal NiNP size, the Ni particle sizes were identical for all catalysts after calcination and reduction treatments. Ultimately, the silica pore sizes determined the final Ni particle size with the Ni redistributed throughout the mesopores, with initially larger particles becoming smaller. This rigid encapsulation ensured that the Ni did not sinter during methanation and should allow for Ni catalysts with high loadings to maintain their dispersion. We expect that this method may be further optimized by changing the silica templating agent to manipulate the pore sizes, thereby controlling the final Ni particle size to achieve catalysts tailored towards specific structure–sensitive reactions.

Conflicts of interest

There are no conflicts of interest to declare.

Acknowledgements

The authors thank NWO and BASF for a TA-CHIPP grant. The authors thank Charlotte Vogt (Utrecht University) for bright-field TEM measurements and Georgy Filonenko (TU Delft) for fruitful discussions. We thank Adelheid Elemans-Mehring (TU Eindhoven) for performing the elemental analysis.

References

1 C.-J. J. Jia and F. Schüth, *Phys. Chem. Chem. Phys.*, 2011, **13**, 2457–2487.
2 M. Cargnello, *Chem. Mater.*, 2019, **31**, 576–596.
3 P. Sonström and M. Bäumer, *Phys. Chem. Chem. Phys.*, 2011, **13**, 19270.
4 P. Losch, W. Huang, E. D. Goodman, C. J. Wrasman, A. Holm, A. R. Riscoe, J. A. Schwalbe and M. Cargnello, *Nano Today*, 2019, **24**, 15–47.
5 R. A. Van Santen, *Acc. Chem. Res.*, 2009, **42**, 57–66.
6 G. L. Bezemer, J. H. Bitter, H. P. C. E. Kuipers, H. Oosterbeek, J. E. Holewijn, X. Xu, F. Kapteijn, A. J. Van Diilen and K. P. De Jong, *J. Am. Chem. Soc.*, 2006, **128**, 3956–3964.
7 M. P. Andersson, F. Abild-Pedersen, I. N. Remediakis, T. Bligaard, G. Jones, J. Engbæk, O. Lytken, S. Horch, J. H. Nielsen and J. Sehested, *J. Catal.*, 2008, **255**, 6–19.
8 C. Vogt, E. Groeneveld, G. Kamsma, M. Nachtegaal, L. Lu, C. J. Kiely, P. H. Berben, F. Meirer and B. M. Weckhuysen, *Nat. Catal.*, 2018, **1**, 127–134.
9 J. Gao, Q. Liu, F. Gu, B. Liu, Z. Zhong and F. Su, *RSC Adv.*, 2015, **5**, 22759–22776.
10 T. S. Rodrigues, A. G. M. da Silva and P. H. C. Camargo, *J. Mater. Chem. A*, 2019, **7**, 5857–5874.
11 P. Munnik, P. E. de Jongh and K. P. de Jong, *Chem. Rev.*, 2015, **115**, 6687–6718.
12 Z. Niu and Y. Li, *Chem. Mater.*, 2014, **26**, 72–83.
13 A. J. F. van Hoof, D. A. J. Michel-Ligthart, H. Friedrich and E. J. M. Hensen, *ChemCatChem*, 2017, **9**, 1018–1024.
14 E. Zacharaki, P. Beato, R. R. Tiruvalam, K. J. Andersson, H. Fjellvåg and A. O. Sjåstad, *Langmuir*, 2017, **33**, 9836–9843.
15 Y. Xia, K. D. Gilroy, H.-C. Peng and X. Xia, *Angew. Chem., Int. Ed.*, 2017, **56**, 60–95.
16 S. Mourdikoudis and L. M. Liz-Marzán, *Chem. Mater.*, 2013, **25**, 1465–1476.
17 H. T. Zhang, G. Wu, X. H. Chen and X. G. Qiu, *Mater. Res. Bull.*, 2006, **41**, 495–501.
18 Y. Chen, D.-L. Peng, D. Lin and X. Luo, *Nanotechnology*, 2007, **18**, 505703.
19 S. Carenco, C. Boissière, L. Nicole, C. Sanchez, P. Le Floch and N. Mézailles, *Chem. Mater.*, 2010, **22**, 1340–1349.
20 F. Davar, Z. Fereshteh and M. Salavati-Niasari, *J. Alloys Compd.*, 2009, **476**, 797–801.
21 E. J. Roberts, S. E. Habas, L. Wang, D. A. Ruddy, E. A. White, F. G. Baddour, M. B. Griffin, J. A. Schaidle, N. Malmstadt and R. L. Brutchey, *ACS Sustainable Chem. Eng.*, 2017, **5**, 632–639.
22 M. Shviro and D. Zitoun, *RSC Adv.*, 2013, **3**, 1380–1387.
23 Y. Chen, X. Luo, H. She, G.-H. Yue and D.-L. Peng, *J. Nanosci. Nanotechnol.*, 2009, **9**, 5157–5163.
24 A. L. Abdelhady, M. A. Malik, P. O'Brien and F. Tuna, *J. Phys. Chem. C*, 2012, **116**, 2253–2259.
25 D. S. Sidhaye, T. Bala, S. Srinath, H. Srikanth, P. Poddar, M. Sastry and B. L. V. Prasad, *J. Phys. Chem. C*, 2009, **113**, 3426–3429.
26 H. Winnischofer, T. C. R. Rocha, W. C. Nunes, L. M. Socolovsky, M. Knobel and D. Zanchet, *ACS Nano*, 2008, **2**, 1313–1319.
27 S. Carenco, D. Portehault, C. Boissière, N. Mézailles and C. Sanchez, *Chem. Rev.*, 2013, **113**, 7981–8065.
28 S. Carenco, Z. Liu and M. Salmeron, *ChemCatChem*, 2017, **9**, 2318–2323.
29 L. M. Moreau, D.-H. Ha, C. R. Bealing, H. Zhang, R. G. Hennig and R. D. Robinson, *Nano Lett.*, 2012, **12**, 4530–4539.
30 R. Rinaldi, A. M. Porcari, T. C. R. Rocha, W. H. Cassinelli, R. U. Ribeiro, J. M. C. Bueno and D. Zanchet, *J. Mol. Catal. A: Chem.*, 2009, **301**, 11–17.
31 V. Iablokov, S. K. Beaumont, S. Alayoglu, V. V. Pushkarev, C. Specht, J. Gao, A. P. Alivisatos, N. Kruse and G. A. Somorjai, *Nano Lett.*, 2012, **12**, 3091–3096.
32 Y. Hou and S. Gao, *J. Mater. Chem.*, 2003, **13**, 1510–1512.
33 H. Li, H. Lin, Y. Hu, H. Li, P. Li and X. Zhou, *J. Mater. Chem.*, 2011, **21**, 18447–18453.

34 D.-H. Chen and C.-H. Hsieh, *J. Mater. Chem.*, 2002, **12**, 2412–2415.
35 Y. Jeon, G. H. Lee, J. Park, B. Kim and Y. Chang, *J. Phys. Chem. B*, 2005, **109**, 12257–12260.
36 R. Eluri and B. Paul, *J. Nanopart. Res.*, 2012, **14**, 800.
37 V. Tzitzios, G. Basina, M. Gjoka, V. Alexandrakis, V. Georgakilas, D. Niarchos, N. Boukos and D. Petridis, *Nanotechnology*, 2006, **17**, 3750–3755.
38 O. Metin, V. Mazumder, S. Özkar and S. Sun, *J. Am. Chem. Soc.*, 2010, **132**, 1468–1469.
39 Ö. Metin, S. Özkar and S. Sun, *Nano Res.*, 2010, **3**, 676–684.
40 Y. Li, J. Wen, A. M. Ali, M. Duan, W. Zhu, H. Zhang, C. Chen and Y. Li, *Chem. Commun.*, 2018, **54**, 6364–6367.
41 D. Laprune, A. Tuel, D. Farrusseng and F. C. Meunier, *ChemCatChem*, 2017, **9**, 2297–2307.
42 F. Goodarzi, L. Kang, F. R. Wang, F. Joensen, S. Kegnaes and J. Mielby, *ChemCatChem*, 2018, **10**, 1566–1570.
43 G. H. Layan Savithra, E. Muthuswamy, R. H. Bowker, B. A. Carrillo, M. E. Bussell and S. L. Brock, *Chem. Mater.*, 2013, **25**, 825–833.
44 S. H. Joo, J. Y. Park, C.-K. Tsung, Y. Yamada, P. Yang and G. A. Somorjai, *Nat. Mater.*, 2009, **8**, 126–131.
45 H. Song, R. M. Rioux, J. D. Hoefelmeyer, R. Komor, K. Niesz, M. Grass, P. Yang and G. A. Somorjai, *J. Am. Chem. Soc.*, 2006, **128**, 3027–3037.
46 A. H. Habibi, R. E. Hayes and N. Semagina, *Catal. Sci. Technol.*, 2018, **8**, 798–805.
47 G. Collins, K. Rahme, J. O'Connell and J. D. Holmes, *Catal. Sci. Technol.*, 2016, **6**, 7212–7219.
48 M. A. Lucchini, A. Testino, A. Kambolis, C. Proff and C. Ludwig, *Appl. Catal., B*, 2016, **182**, 94–101.
49 J. Zhang and F. Li, *Appl. Catal., B*, 2015, **176–177**, 513–521.
50 J. Pu, K. Nishikado, N. Wang, T. T. Nguyen, T. Maki and E. W. Qian, *Appl. Catal., B*, 2018, **224**, 69–79.
51 Y. Koltypin, A. Fernandez, T. C. Rojas, J. Campora, P. Palma, R. Prozorov and A. Gedanken, *Chem. Mater.*, 1999, **11**, 1331–1335.
52 M. Feygenson, A. Kou, L. E. Kreno, A. L. Tiano, J. M. Patete, F. Zhang, M. S. Kim, V. Solovyov, S. S. Wong and M. C. Aronson, *Phys. Rev. B: Condens. Matter Mater. Phys.*, 2010, **81**, 014420.
53 L. He, *J. Magn. Magn. Mater.*, 2010, **322**, 1991–1993.
54 Y. Goto, K. Taniguchi, T. Omata, S. Otsuka-Yao-Matsuo, N. Ohashi, S. Ueda, H. Yoshikawa, Y. Yamashita, H. Oohashi and K. Kobayashi, *Chem. Mater.*, 2008, **20**, 4156–4160.
55 Z. L. Schaefer, K. M. Weeber, R. Misra, P. Schiffer and R. E. Schaak, *Chem. Mater.*, 2011, **23**, 2475–2480.
56 P. Hooker, B. J. Tan, K. J. Klabunde and S. Suib, *Chem. Mater.*, 1991, **3**, 947–952.
57 Y. Leng, Y. Liu, X. Song and X. Li, *J. Nanosci. Nanotechnol.*, 2008, **8**, 4477–4481.
58 B. C. Bayer, D. A. Bosworth, F. B. Michaelis, R. Blume, G. Habler, R. Abart, R. S. Weatherup, P. R. Kidambi, J. J. Baumberg, A. Knop-Gericke, R. Schloegl, C. Baehtz, Z. H. Barber, J. C. Meyer and S. Hofmann, *J. Phys. Chem. C*, 2016, **120**, 22571–22584.
59 Y. Leng, L. Xie, F. Liao, J. Zheng and X. Li, *Thermochim. Acta*, 2008, **473**, 14–18.
60 J. Park, E. Kang, S. U. Son, H. M. Park, M. K. Lee, J. Kim, K. W. Kim, H.-J. Noh, J.-H. Park, C. J. Bae, J.-G. Park and T. Hyeon, *Adv. Mater.*, 2005, **17**, 429–434.
61 V. K. LaMer and R. H. Dinegar, *J. Am. Chem. Soc.*, 1950, **72**, 4847–4854.
62 J. Polte, *CrystEngComm*, 2015, **17**, 6809–6830.
63 P. Burattin, M. Che and C. Louis, *J. Phys. Chem. B*, 1997, **101**, 7060–7074.
64 J. C. Park, H. J. Lee, J. U. Bang, K. H. Park and H. Song, *Chem. Commun.*, 2009, 7345–7347.
65 C. K. Vance and C. H. Bartholomew, *Appl. Catal.*, 1983, **7**, 169–177.
66 C. H. Batholomew and C. K. Vance, *J. Catal.*, 1985, **91**, 78–84.
67 G. D. Weatherbee and C. H. Bartholomew, *J. Catal.*, 1981, **68**, 67–76.
68 M. A. A. Aziz, A. A. Jalil, S. Triwahyono, R. R. Mukti, Y. H. Taufiq-Yap and M. R. Sazegar, *Appl. Catal., B*, 2014, **147**, 359–368.
69 G. Garbarino, P. Riani, L. Magistri and G. Busca, *Int. J. Hydrogen Energy*, 2014, **39**, 11557–11565.
70 M. C. Bacariza, I. Graça, S. S. Bebiano, J. M. Lopes and C. Henriques, *Chem. Eng. Sci.*, 2018, **175**, 72–83.
71 J. R. A. Sietsma, J. D. Meeldijk, M. Versluijs-Helder, A. Broersma, A. J. van Dillen, P. E. de Jongh and K. P. de Jong, *Chem. Mater.*, 2008, **20**, 2921–2931.